

**Superior performance of FeVO<sub>4</sub>@CeO<sub>2</sub> uniform core-shell nanostructures in heterogeneous Fenton-sonophotocatalytic degradation of 4-nitrophenol**

Eshaq Gh., Wang Shaobin, Sun Hongqi, Sillanpää Mika

This is a Final draft version of a publication  
published by Elsevier  
in Journal of Hazardous Materials

**DOI:** 10.1016/j.jhazmat.2019.121059

**Copyright of the original publication:** © 2019 Elsevier B.V.

**Please cite the publication as follows:**

Eshaq, Gh., Wang, S., Sun, H., Sillanpää, M. (2020). Superior performance of FeVO<sub>4</sub>@CeO<sub>2</sub> uniform core-shell nanostructures in heterogeneous Fenton-sonophotocatalytic degradation of 4-nitrophenol. Journal of Hazardous Materials, vol. 382. DOI: 10.1016/j.jhazmat.2019.121059

**This is a parallel published version of an original publication.  
This version can differ from the original published article.**

# Superior performance of FeVO<sub>4</sub>@CeO<sub>2</sub> uniform core-shell nanostructures in heterogeneous Fenton-sonophotocatalytic degradation of 4-nitrophenol

Gh. Eshaq<sup>a,b\*</sup>, Shaobin Wang<sup>c</sup>, Hongqi Sun<sup>d</sup>, Mika Sillanpää<sup>a</sup>

<sup>a</sup> Department of Green Chemistry (DGC), School of Engineering Science, Lappeenranta University of Technology, Sammonkatu 12, FI-50130, Mikkeli, Finland

<sup>b</sup> Petrochemicals department, Egyptian Petroleum Research Institute, Nasr City, Cairo 11727, Egypt

<sup>c</sup> School of Chemical Engineering, The University of Adelaide, Adelaide, SA 5005, Australia.

<sup>d</sup> School of Engineering, Edith Cowan University, Perth, WA 6027, Australia.

## Abstract

Porous FeVO<sub>4</sub> nanorods decorated on CeO<sub>2</sub> nanocubes (FeVO<sub>4</sub>@CeO<sub>2</sub>) were successfully prepared via a facile hydrothermal route and tested in the degradation of 4-nitrophenol (4-NP) for enhanced heterogeneous oxidation using ultrasonic (US), ultraviolet (UV), and binary irradiation US/UV, respectively. The nanostructure of the core-shell FeVO<sub>4</sub>@CeO<sub>2</sub> was characterised using XRD, SEM, EDS elemental mapping, TEM, HRTEM, SAED, FTIR, Raman, BET, point of zero charge (PZC), XPS analysis and UV-vis DRS. The effect of various parameters, for examples, nanostructured core-shell amounts, hydrogen peroxide concentration, initial concentration, pH and irradiation time, on 4-NP degradation were investigated for the optimisation of the catalytic performance. The durability and stability of the core-shell nanostructured materials were also investigated and the obtained results revealed that the catalysts can endure the harsh sonophotocatalytic conditions even after six cycles. Mineralisation experiments were investigated using the optimised parameters. The core-shell nanostructured FeVO<sub>4</sub>@CeO<sub>2</sub> has higher PZC than pure FeVO<sub>4</sub> and CeO<sub>2</sub>, leading to excellent sonophotocatalytic activity even at high pH and stability for the degradation of 4-NP after six cycles. A possible mechanism over the FeVO<sub>4</sub>@CeO<sub>2</sub> was proposed based on the special three-

way Fenton-like mechanism and the dissociation of H<sub>2</sub>O<sub>2</sub> with the experiments of active species trapping and calculated band gap energy.

**Keywords:** Core/shell, sonophotocatalysis, synergy index, semiconductor, 4-nitrophenol

## 1. Introduction

Nitro aromatics have been widely used in the manufacture of many chemical products like pharmaceuticals, dyes, solvents, explosives and fungicidal agents [1, 2]. Nevertheless, these nitro compounds have serious effects on the environment and also a highly toxic effect on living organisms [3]. Among these compounds, 4-nitrophenol (4-NP) is used as a chemical intermediate for rubber, lumber preservatives, azo and others [4]. According to the USA Environmental Protection Agency (EPA), 4-NP has been classified as a priority toxic pollutant [5]. Advanced Oxidation Processes (AOPs), are considered as the most promising approaches to the destruction of recalcitrant organic pollutants, and are based on the generation of hydroxyl radicals [6]. Recently, sonolysis with an appropriate catalyst has received great attention as a promising system owing to the generation of more free radicals [7, 8].

Nevertheless, it has been observed that a combination of different AOPs has been found to be more efficient and foster the degree of mineralisation of organic pollutants [9, 10]. It has been reported that the simultaneous use of sonolysis and photocatalysis called sonophotocatalysis can be considered a promising technique with increasing the production of •OH radicals [11,12].

Nowadays, the core-shell nanostructure have great potential in catalysis because of their unique chemical and physical characteristics and have many advantages such as an increased number of surface-active sites for the core and promotion by the shell of catalytic activity [13,

14]. Moreover, the reactions of all catalysts occur at the same time and the strength of the shell can protect the core and prevent assemblage of the particles [15, 16]. In this context, many researchers have used various core shell nanostructures [17-31]. Among the inorganic shell materials, cerium oxide ( $\text{CeO}_2$ ) has served as one of the most efficient photocatalysts for the degradation of organic pollutants because of its ability to transform between  $\text{Ce}^{+3}$  and  $\text{Ce}^{+4}$  states at oxygen vacancy sites, and to facilitate electron transfer and  $e^-/h^+$  pair diffusion between  $\text{CeO}_2$  and another semiconductor such as  $\text{Cu}_2\text{O}$  [32],  $\text{CdS}$  [33] and  $\text{TiO}_2$  [34, 35]. Accordingly, the preparation of core-shell materials with a metal as a core and ceria as a shell is of great significance. Iron vanadate  $\text{FeVO}_4$  is considered as a semiconducting, highly stable, selective as a photocatalyst accordingly to its unique and excellent performance [36].

To the best of our knowledge, successful synthesis of a  $\text{FeVO}_4@ \text{CeO}_2$  core shell nanostructure and its use as heterogenous Fenton-like catalyst in the degradation of 4-NP in the presence of ultrasonic (US), ultraviolet (UV), and binary irradiation US/UV, using  $\text{H}_2\text{O}_2$  as an oxidant have not been reported. In this work, a  $\text{FeVO}_4@ \text{CeO}_2$  was synthesized and investigated with XRD, SEM, EDS, TEM, HRTEM, SAED, FTIR, Raman,  $\text{N}_2$ -adsorption-desorption, DRS and XPS. The different degradation parameters, for instance, irradiation time, catalyst loading, pH and  $\text{H}_2\text{O}_2$  initial concentration were optimized, and the mineralization and recyclability were examined. Moreover, the synergistic effect with reaction kinetics was investigated in detail and the possible mechanism was discussed.

## **2. Experimental**

### *2.1. Catalysts preparation*

#### *2.1.1 Preparation of porous $\text{FeVO}_4$ nanorods*

$\text{FeCl}_3 \cdot 6\text{H}_2\text{O}$  (2 mmol) was dissolved in 10 mL of deionised water and  $\text{NH}_4\text{VO}_3$  (2 mmol) was dissolved in another 10 mL of deionised water at 90 °C. Next,  $\text{NH}_4\text{VO}_3$  solution was slowly added to  $\text{FeCl}_3 \cdot 6\text{H}_2\text{O}$  solution under constant stirring. After 20 min of stirring, the obtained slurry was placed in a 50 mL Teflon-lined stainless-steel autoclave. The autoclave was sealed and heated at 180 °C for 3 h and then left to cool down naturally to the ambient temperature. The obtained precipitate was separated by centrifugation, washed with deionised water and absolute ethanol several times, and then dried in an oven at 60 °C for 6 h. After drying, the obtained powder was calcined at 500 °C at a rate of 5 °C/min for 2 h [37].

### *2.1.2. Preparation of $\text{CeO}_2$ nanocubes*

$\text{CeO}_2$  nanocubes were prepared using an ultrasonic-assisted precipitation method as described in [38].  $\text{Ce}(\text{NO}_3)_3 \cdot 6\text{H}_2\text{O}$  (0.1 M) and NaOH (0.3 M) solutions were prepared and the NaOH solution was added dropwise to the cerium nitrate solution under sonication. After that, the slurry was kept under sonication for 60 min. The obtained yellowish precipitates of cerium hydroxide were separated by centrifugation, washed with deionised water several times and then calcined at 250 °C for 4 h.

### *2.1.3. Preparation of $\text{FeVO}_4@ \text{CeO}_2$ core shell nanostructures*

$\text{FeVO}_4@ \text{CeO}_2$  core shell nanostructures were prepared using a hydrothermal route, where 0.1 g of  $\text{FeVO}_4$  as-prepared, 0.5 g of  $\text{CO}(\text{NH}_2)_2$ , 0.2 g of  $\text{CeCl}_3$ , and 1.0 g (PVP,  $M_w = 58,000$ ) were added to 80 mL of ethanol (50%, V/V) under continuous stirring for 6 h. The suspension was placed in a 50 mL Teflon-lined stainless-steel autoclave that was heated at 110 °C for 20 h and then left to cool down naturally to the ambient temperature. The obtained  $\text{FeVO}_4@ \text{CeO}_2$  was collected by centrifugation, washed several times in deionised water and absolute ethanol, dried in an oven at 50 °C for 12 h and then calcined at 500 °C for 4 h [39].

## *2.2. Characterisation*

The crystalline phase was investigated by XRD analysis on a PANalytical diffractometer with Cu K $\alpha$  radiation (wave-length = 1.54 Å) operated at 40 kV and 40 mA. SEM with energy dispersive X-ray spectroscopy (HITACHI /EDS S-4800) attached was used. TEM, HRTEM and SAED were measured on a JEOL JEM-2010 (HT) operated at 200 kV. FTIR spectrum (Bruker Platinum ATR VERTEX 70) and Raman analysis were measured using a Horiba Jobin Yvon, and a Labram HR, respectively. Surface texture parameters (BET) were measured by nitrogen adsorption/desorption using a MicroActive-TriStar II Plus 2.03. The PZC was determined using the mass titration method [40]. XPS was done on an ESCALAB 250Xi with Al-K (1486.6 eV). DRS was done on an Agilent Cary 5000 UV-Vis spectrometer with a DRA 2500 integrating sphere.

## *2.3. Sonophotocatalytic reactor and experimental procedures*

Ultrasonic experiments were performed in programmable sonication at an ultrasound frequency of 20 kHz (Sonics & Materials, Inc., VCX 750) with a titanium alloy probe with a tip diameter of 13 mm and maximum power output of 125 W. Water circulation was used to maintain the reaction temperature at  $25 \pm 2$  °C. The quartz reactor was filled with 110 mL 4-NP solution for each experiment, followed by a dispersed specific amount of the prepared catalyst to the solution. The reaction was initiated once adding H<sub>2</sub>O<sub>2</sub>. The obtained samples were analysed using an HPLC (SHIMADZU®) equipped with a Phenomenex® C18 column (5  $\mu$ m, 150 mm  $\times$  4.6 mm) and a UV detector adjusted to 285 nm. A mixture of acetonitrile and Milli-Q water with a volumetric ratio of 50:50 was used as the mobile phase throughout the analysis with

a flow rate of 1 mLmin<sup>-1</sup>. A Total Organic Carbon Analyzer (TOC-VCPH Shimadzu) equipped with an auto sampler (ASI-V Shimadzu).

### **3. Results and discussion**

#### *3.1. Characteristics of the prepared FeVO<sub>4</sub>@CeO<sub>2</sub> core shell nanostructure*

##### *3.1.1. XRD*

The crystalline phases and composition of pure FeVO<sub>4</sub>, CeO<sub>2</sub> and FeVO<sub>4</sub>@ CeO<sub>2</sub> were determined by XRD analysis (Fig. 1). The porous FeVO<sub>4</sub> nanorods present a similar XRD pattern to the triclinic FeVO<sub>4</sub> (JCPDS No. 71- 1592). Further, CeO<sub>2</sub> prepared ultrasonically shows all the diffraction peaks matched very well with the nanoceria of cubic fluorite structure (JCPDS No. 75-0390). The diffraction pattern of the FeVO<sub>4</sub>@CeO<sub>2</sub> shows that all the peaks are in good agreement with the peaks of the triclinic structure of the FeVO<sub>4</sub> and of cubic CeO<sub>2</sub> nanoparticles. The decrease intensities in the diffraction peaks of FeVO<sub>4</sub> were observed as a result of CeO<sub>2</sub> coating. The average crystallite sizes calculated using the Scherrer equation of FeVO<sub>4</sub>, CeO<sub>2</sub> and FeVO<sub>4</sub>@CeO<sub>2</sub> are 45, 20 and 78 nm, respectively.

##### *3.1.2. SEM - EDS with elemental mapping*

To obtain insights into the morphology and surface features of the prepared samples, we carried out SEM analysis. Figs. 2(a-c) show the SEM of the individual FeVO<sub>4</sub>, CeO<sub>2</sub> and FeVO<sub>4</sub>@CeO<sub>2</sub> core shell nanostructure, respectively. Fig. 2a shows that the morphology of FeVO<sub>4</sub> is in porous nanorod-type with smooth surfaces. Fig. 2b shows that CeO<sub>2</sub> has a flower-like structure. The SEM image of FeVO<sub>4</sub>@ CeO<sub>2</sub> in Fig 2c, shows the core-shell nanostructure, where the porous nanorod particles of FeVO<sub>4</sub> are shielded by a thin layer of CeO<sub>2</sub> particles. To

confirm the core-shell nanostructure and the distribution of the elements in the core-shell nanostructure, Fig. 2(d-i) shows the EDX spectrum of FeVO<sub>4</sub>@CeO<sub>2</sub> and EDS mapping.

### 3.1.3. TEM, HRTEM and SAED

Figs. 3 (a-c) show the TEM images of FeVO<sub>4</sub>, CeO<sub>2</sub> and FeVO<sub>4</sub>@CeO<sub>2</sub>, respectively. The morphology of FeVO<sub>4</sub> shows porous nanorods with an average diameter of 45-50 nm, whereas CeO<sub>2</sub> is cube-shaped particle with an average size of 15-20 nm, which agrees with the data calculated by the Scherrer equation. Based on the TEM image, the shell thickness was determined to be 25 nm.

The corresponding SAED patterns of FeVO<sub>4</sub>, CeO<sub>2</sub> and FeVO<sub>4</sub>@CeO<sub>2</sub> in Figs. 3(d-f) endorse the presence of single crystalline phase of triclinic FeVO<sub>4</sub>, cubic fluorite CeO<sub>2</sub> and their mixture. Fig.3 (g) shows the HRTEM image of the heterojunction area between FeVO<sub>4</sub> and CeO<sub>2</sub> in FeVO<sub>4</sub>@CeO<sub>2</sub>, illustrating the presence of two sets of different interplanar spacing. The lattice fringes of 0.624 and 0.278 nm correspond to the interplanar spacing of (111) and (112) planes of triclinic FeVO<sub>4</sub> phase, respectively, while the interplanar spacing of 0.318 and 0.265 nm matches well with the fringe spacing of (111) and (200) lattice planes of the cubic fluorite CeO<sub>2</sub> structure, respectively.

### 3.1.4. FTIR

FTIR analysis for FeVO<sub>4</sub>, CeO<sub>2</sub> and FeVO<sub>4</sub>@CeO<sub>2</sub> was carried out and the obtained spectra are presented in Fig 4. The bands at 3,400 and 1,630 cm<sup>-1</sup> are ascribed to the OH stretching vibrations of the absorbed water molecules. For FeVO<sub>4</sub>, the bands appearing at 880 and 1,050 cm<sup>-1</sup> are ascribed to the terminal V-O stretching vibrations. The presence of bands at 700–800 cm<sup>-1</sup> is an indication of the bridging V-O...Fe stretching vibration [41] while those

appearing at 550–700  $\text{cm}^{-1}$  are ascribed to mixed bridging V–O...Fe and V...O...Fe stretching. These data concur well with the previously published data [42]. The FTIR spectrum of  $\text{CeO}_2$  exhibits a strong broad band at 550  $\text{cm}^{-1}$  ascribed to the stretching vibration of Ce–O [43]. It is clear that this band became broader in the  $\text{FeVO}_4@ \text{CeO}_2$  spectrum and can be ascribed to the overlapping between the V–O...Fe band and Ce–O band.

### 3.1.5. Raman

Further evidence of core shell formation in  $\text{FeVO}_4@ \text{CeO}_2$  nanostructures is revealed by Raman spectroscopy. The Raman spectra of  $\text{FeVO}_4$ ,  $\text{CeO}_2$  and  $\text{FeVO}_4@ \text{CeO}_2$  core shell nanostructures are shown in Fig. 5. The Raman spectrum of  $\text{FeVO}_4$  shows the characteristic bands of  $\text{FeVO}_4$ , which revealed that the peaks between (970–895  $\text{cm}^{-1}$ ), are assigned to the terminal V–O stretching, and those appear at (890–736  $\text{cm}^{-1}$ ) corresponding to the bridging V–O–Fe stretching, while the peaks between (730–633  $\text{cm}^{-1}$ ) corresponding to the mixed bridging V–O–Fe and V–O–Fe stretching and the bands observed at (502–317  $\text{cm}^{-1}$ ) are attributed to V–O–V deformations and Fe–O stretching [44]. In the case of the Raman spectrum of  $\text{CeO}_2$  exhibit a sharp band at 463  $\text{cm}^{-1}$  is assigned to the  $\text{F}_2\text{g}$  modes of  $\text{CeO}_2$ , thus confirming the cubic fluorite structure [45]. The Raman spectrum of  $\text{FeVO}_4@ \text{CeO}_2$  exhibits all the characteristic bands of  $\text{FeVO}_4$  and  $\text{CeO}_2$  with a slight decrease in the intensity of the bands assigned to  $\text{FeVO}_4$ , which can be attributed to the coverage of  $\text{FeVO}_4$  nanoparticles with  $\text{CeO}_2$  nanoparticles.

### 3.1.6. BET

Texture analysis of  $\text{FeVO}_4$ ,  $\text{CeO}_2$  and  $\text{FeVO}_4@ \text{CeO}_2$  were performed and the surface areas ( $S_{\text{BET}}$ ) and total pore volumes ( $V_p$ ) are listed in Table 1. The isotherms of all the catalysts (Fig.6) are of type IV with a hysteresis loop of type H3 [46], confirming that the pore size is

mainly in the range of mesopore [47]. As shown in Fig.6 (inset) and Table 1, the pores of the catalysts are in good agreement with the mesoporous structure. The  $S_{\text{BET}}$  values of  $\text{FeVO}_4$  and  $\text{CeO}_2$  are 24.2 and 20.5  $\text{m}^2\text{g}^{-1}$ , respectively, while the value of  $\text{FeVO}_4@\text{CeO}_2$  is 27.5  $\text{m}^2\text{g}^{-1}$ , larger than that of  $\text{FeVO}_4$  and  $\text{CeO}_2$ . Moreover,  $\text{FeVO}_4@\text{CeO}_2$  also displays nearly two times greater pore volume ( $0.062 \text{ cm}^3\text{g}^{-1}$ ) than  $\text{FeVO}_4$  ( $0.032 \text{ cm}^3\text{g}^{-1}$ ) and  $\text{CeO}_2$   $0.032 \text{ cm}^3\text{g}^{-1}$ . The larger ( $S_{\text{BET}}$ ) and ( $V_p$ ) of  $\text{FeVO}_4@\text{CeO}_2$  increase the number of active sites and enhance the reactant mass transfer.

### 3.1.7. DRS

UV-vis diffuse reflectance spectroscopy (DRS) was performed to obtain the light absorption properties of  $\text{FeVO}_4$ ,  $\text{CeO}_2$ , and  $\text{FeVO}_4@\text{CeO}_2$  in the range of 250 - 800 nm (Fig. 7(a)). The values of the band gap energy of  $\text{FeVO}_4$ ,  $\text{CeO}_2$ , and  $\text{FeVO}_4@\text{CeO}_2$  were determined to be 1.95, 2.76 and 1.91 eV, respectively, as shown in Fig. 7(a). It can be seen that the absorption edge of the  $\text{FeVO}_4@\text{CeO}_2$  exhibits a shift toward the visible region with a band gap energy ( $E_g$ ), lower than that of  $\text{FeVO}_4$  and  $\text{CeO}_2$  due to the heterojunction structure, and defect states induced by oxygen vacancies [48] that leads to the formation of  $\text{Ce}^{3+}$  from  $\text{Ce}^{4+}$ . This increase in the amount of  $\text{Ce}^{3+}$  states leads to the formation of localised energy states, which are closer to the conduction band and thereby decreasing the band gap [49]. In addition, oxygen vacancies and  $\text{Ce}^{3+}$  form intermediate defect energy states in the band gap. These intermediate energy states lead to retarding in the direct transition of photoinduced electrons from the valence band (VB) to the conduction band (CB), which in turn narrows the band gap [50]. The transition character of the absorption edge (direct or indirect) was evaluated by plotting the square and square root of absorption coefficient against energy and then determining the linear one and the

one that deviates away from the straight line [51]. The data reveal that the absorption edge of all the samples is caused by indirect transitions as shown in Fig. 7(b).

### 2.1.8. XPS

The composition and valance states of  $\text{FeVO}_4@\text{CeO}_2$  were investigated by XPS analysis (Fig.8).The survey XPS spectrum of  $\text{FeVO}_4@\text{CeO}_2$  in Fig. 8(a) is composed primarily of peaks from C, Fe, O, V, and Ce. The C 1s peak at about 284.5 eV is attributed to the signal from carbon in the instrument and was used for calibration [52]. As shown in Fig. 8(b), the peaks at 723.65 and 710.4 eV correspond to the Fe  $2p_{1/2}$  and Fe  $2p_{3/2}$  signals of  $\text{Fe}^{3+}$  species [53]. It can be clearly seen from Fig.8(c) that the doublet peaks located at V  $2p_{1/2}$  and  $2p_{3/2}$  peaks at 525.2 and 516.9 eV, respectively, are attributed to  $\text{V}^{5+}$  in  $\text{FeVO}_4$  [54], and that the peak for O 1s located at about 531.77 eV is due to the formation of O-H bonds [55]. From Fig. 8(d) the main peaks attributed to  $\text{Ce}^{4+}$   $3d_{5/2}$  and  $\text{Ce}^{4+}$   $3d_{3/2}$  are observed at the binding energies of 898.57 and 916.85 eV, respectively [56]. The presence of  $\text{Ce}^{3+}$   $3d_{5/2}$  is observed at 882.73 eV. In addition to these, two peaks are observed at 890.45 and 908.89 eV, corresponding to the presence of  $\text{Ce}^{3+}$   $3d_{5/2}$  and  $\text{Ce}^{3+}$   $3d_{3/2}$ , respectively [57]. These results reveal the formation of a mixed valence state of cerium species of  $\text{Ce}^{3+}$  and  $\text{Ce}^{4+}$  in the  $\text{FeVO}_4@\text{CeO}_2$ . Moreover, the increase of  $\text{Ce}^{3+}$  species increases the oxygen vacancies around  $\text{Ce}^{4+}$ , leading to the achievement of equilibrium charge in the catalysts [58].

## 3.2. Insights in degradation of 4-NP using ultrasonic or ultraviolet irradiations in the presence of $\text{FeVO}_4@\text{CeO}_2$

### 3.2.1. Effect of sonolysis or photolysis conditions

To investigate the capability of (US) irradiation and (UV) irradiation on the degradation of 4-NP, the sonolysis and photolysis of 4-NP solutions were carried out in the absence of any oxidant or catalyst as shown in Fig.S1. The obtained results revealed that the degradation extent reached 16% and 27% after 1 h of sonolysis and photolysis, respectively. This degradation capability can be ascribed to the generation of different free radicals [59, 60] as a result of the photolysis or sonolysis of 4-NP aqueous solutions. The effect of H<sub>2</sub>O<sub>2</sub> concentration on the sonolysis and photolysis of 4-NP was tested in a range of 5-40 mM (Fig.S2). The addition of H<sub>2</sub>O<sub>2</sub> enhanced the degradation performance of the sonolysis and photolysis of 4-NP reaching 38% and 50%, respectively, up to 20 mM H<sub>2</sub>O<sub>2</sub>, and after this concentration the degradation efficiency declined. This enhanced performance attributed to the production of extra amounts of free radicals and also because the ultrasonic-assisted cleavage of the O-O bond in H<sub>2</sub>O<sub>2</sub> is much easier than O-H bond in water [61]. However, the use of the extravagant H<sub>2</sub>O<sub>2</sub> scavenges the free radicals generated instead of generating additional radicals [62].

### *3.2.2. Optimisation of ultrasonic or photo-heterogeneous Fenton*

In the absence of any irradiation (US or UV), called (silent mode), several catalytic runs were performed. It has been observed that the extent of degradation was only 9% for 4-NP (20 ppm) using 40 mM H<sub>2</sub>O<sub>2</sub>, 0.1 g of the catalyst and pH 7 with continuous stirring for 1 h.

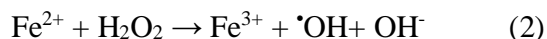
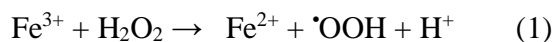
#### *3.2.2.1. Optimisation of sonocatalytic or photocatalytic irradiation time*

The FeVO<sub>4</sub>@CeO<sub>2</sub> was introduced as heterogeneous Fenton like to the sonolysis or photolysis systems in the presence of H<sub>2</sub>O<sub>2</sub> to enhance the degradation performance of the systems. The effect of irradiation time was investigated and the obtained data are presented in Fig. S3. The results demonstrate that using 0.1 g L<sup>-1</sup> of FeVO<sub>4</sub>@CeO<sub>2</sub>, 10 mM of H<sub>2</sub>O<sub>2</sub>, 4-NP

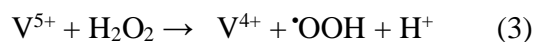
(20 ppm), pH 7 and 1 h time for irradiation, a degradation extent of 85% and 94% was achieved for sonocatalytic or photocatalytic irradiation respectively.

### 3.2.2.1.1. Mechanistic insights into the sonocatalytic degradation of 4-NP over FeVO<sub>4</sub>@CeO<sub>2</sub>

To gain a full understanding of the sonocatalysis mechanism of 4-NP over the FeVO<sub>4</sub>@CeO<sub>2</sub>, the mechanism of Fenton-like reaction was studied. The catalytic mechanism possibly involved, in a special three-way Fenton-like mechanism, the dissociation of H<sub>2</sub>O<sub>2</sub> by both Fe<sup>3+</sup> and V<sup>5+</sup> in FeVO<sub>4</sub> as the first and second pathway and Ce<sup>4+</sup> in CeO<sub>2</sub> as the third pathway. The Fe<sup>3+</sup> ions are able to react with H<sub>2</sub>O<sub>2</sub> to generate an intermediate complex (Fe–O<sub>2</sub>H<sub>2</sub><sup>+</sup>) that can be dissociated into Fe<sup>2+</sup> and HO<sub>2</sub><sup>•</sup> under (US) irradiation. Fe<sup>2+</sup> ions are able to react with H<sub>2</sub>O<sub>2</sub> to generate a higher concentration of <sup>•</sup>OH. The first pathway of the Fenton-like reaction is illustrated as follows [63]:

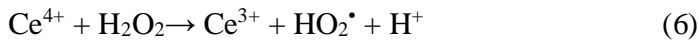
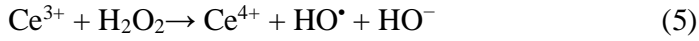


The activation of V<sup>5+</sup> in FeVO<sub>4</sub> with H<sub>2</sub>O<sub>2</sub> to generate <sup>•</sup>OH as the second pathway is described in the following eq. [64-65]:



It should be noted that the recycling of Fe<sup>3+</sup> from Fe<sup>2+</sup> in eq (2) and V<sup>5+</sup> from V<sup>4+</sup> in eq (4) is much slower than the reactions in eq (1) and in eq (3), respectively. Thus, we believed that these two redox cycles (Fe<sup>3+</sup>/Fe<sup>2+</sup> and V<sup>5+</sup>/V<sup>4+</sup>) take place within the FeVO<sub>4</sub>–H<sub>2</sub>O<sub>2</sub> system. Furthermore, the redox cycle of CeO<sub>2</sub> between Ce<sup>3+</sup> and Ce<sup>4+</sup> as the third pathway makes it a

potential candidate as a heterogeneous Fenton-like and thus can be employed efficiently in the degradation of reluctant organic contaminants [66]. Heckert et al. [67] reported that CeO<sub>2</sub> is able to generate considerable numbers of HO• in the presence of H<sub>2</sub>O<sub>2</sub> as an oxidant, which is similar to that generated in an iron Fenton-like reaction according to the following eqs. :



### 3.2.2.1.2. Mechanistic insights into photocatalytic degradation of 4-NP over FeVO<sub>4</sub>@CeO<sub>2</sub>

Based on the calculated band energy and data from the scavenging of the active species experiments above, a type-II staggered-gap type of heterojunction structure is formed between FeVO<sub>4</sub> and CeO<sub>2</sub> with tunable band edge potentials. The band edge positions for the semiconductor of both (CB) and (VB) at the value of PZC could be determined according to the following equations [68-69]:

$$E_{\text{CB}} = \chi - E_e - 1/2E_g \quad (7)$$

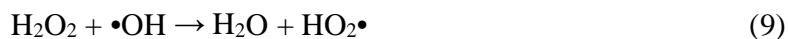
$$E_{\text{VB}} = E_g + E_{\text{CB}} \quad (8)$$

where  $\chi$  represents the semiconductor's absolute electronegativity;  $E_e$  represents the free electrons energy on the hydrogen scale (ca. 4.5 eV); and  $E_g$  represents the semiconductor's band gap energy. The calculated values of both CB and VB of FeVO<sub>4</sub> are -0.44 and 1.56 eV, and those of CeO<sub>2</sub> are -0.32 and 2.44 eV, respectively. The possible mechanism was proposed under UV light irradiation; both FeVO<sub>4</sub> and CeO<sub>2</sub> can be activated since the VB and CB of CeO<sub>2</sub> are more negative than those calculated for FeVO<sub>4</sub>. Thus, the excited electrons in the CB of CeO<sub>2</sub> transfer

readily to the CB of FeVO<sub>4</sub>. Also, the holes in the VB of FeVO<sub>4</sub> transfer directly to the VB of CeO<sub>2</sub>. Such transitions in the heterojunction core-shell nanostructure afford substantial suppression in the e<sup>-</sup>/h<sup>+</sup> pair recombination and also prolong the lifetime of the carriers. Moreover, this heterojunction structure in the presence of H<sub>2</sub>O<sub>2</sub> can change the electronic structure and oxidation states of V<sup>4+</sup>/V<sup>5+</sup> and Ce<sup>3+</sup>/Ce<sup>4+</sup>. The V<sup>4+</sup>/V<sup>5+</sup> pairs are able to form energy state deficiency, which can act as an e<sup>-</sup>/h<sup>+</sup> trap and thus suppress the rate of recombination [70]. Moreover, the surface Ce<sup>4+</sup> ions are able to trap the electrons in the CB where they are reduced to Ce<sup>3+</sup> ions. These reduced ions (Ce<sup>3+</sup>) are able to react with the dissolved oxygen to produce superoxide radicals (<sup>•</sup>O<sub>2</sub><sup>-</sup>) and some of them may be re-oxidised again to Ce<sup>4+</sup> using the generated holes or hydroxyl radicals to complete a cycle reaction. Thus, the existence of Ce<sup>3+</sup>/Ce<sup>4+</sup> pairs not only effectively delays the e<sup>-</sup>/h<sup>+</sup> pair recombination but also plays a role in the generation of <sup>•</sup>O<sub>2</sub><sup>-</sup> [71]. Meanwhile, <sup>•</sup>OH are formed by oxidising the absorbed OH<sup>-</sup> and H<sub>2</sub>O using the holes in the VB of CeO<sub>2</sub> [72]. Scheme 1 shows a mechanism of various radical generations over FeVO<sub>4</sub>@CeO<sub>2</sub> core shell nanostructures in a sonophotocatalytic system for the degradation of 4-NP.

#### 3.2.2.2. Optimisation of H<sub>2</sub>O<sub>2</sub> concentration

To gain insight into the effects of H<sub>2</sub>O<sub>2</sub> concentration on 4-NP degradation on FeVO<sub>4</sub>@CeO<sub>2</sub>, the addition of H<sub>2</sub>O<sub>2</sub> in a range of 5–40 mM was examined. It was observed that an increase in sonocatalytic degradation and photocatalytic degradation of 4-NP in the range of 5 and 15 mM of H<sub>2</sub>O<sub>2</sub> as shown in Fig.S4. It is obvious that, as the concentration of H<sub>2</sub>O<sub>2</sub> increases, the extent of degradation of 4-NP increases up to an optimum concentration and then decreases. This is due to the scavenger effects of H<sub>2</sub>O<sub>2</sub>, which are illustrated by Eq. (9) and (10) [16].



On the other hand, the addition of  $\text{H}_2\text{O}_2$  also acts as an electron trap and is able to suppress the  $e^-/h^+$  recombination [73], as can be described in Eq. (11), (12):



### 3.2.2.3. Optimisation of catalyst amount

To unfold the role of catalyst amount on the degradation of 4-NP, different catalyst amounts in the range of 0.05-1 g L<sup>-1</sup> of FeVO<sub>4</sub>@CeO<sub>2</sub> were tested as shown in Fig.S5 for (US) and (UV) irradiation. The obtained results revealed that, as the amounts of catalyst increases, the degradation efficiency increases up to 0.3 g L<sup>-1</sup> for (UV) and (US) irradiation and then begin to decrease slowly with a further increase in the catalyst amount. Due to the increase in the number of obtainable active sites, induces H<sub>2</sub>O<sub>2</sub> decomposition and enhances the generation rate of cavitation bubbles and subsequently generates more hydroxyl radicals [19, 74]. On the other hand, the decrease in the degradation efficiency by increasing the amount of the catalyst can be ascribed to the dissipation of the (US) irradiation by the agglomerated catalyst, [75, 76] and also prevents the (UV) irradiation from illuminating the catalyst particles [77].

### 3.3. Optimisation of the sonophotocatalytic degradation of 4-NP using FeVO<sub>4</sub>@CeO<sub>2</sub>

All the optimised conditions of the sonocatalytic and photocatalytic reactions were carefully selected and applied in the sonophoto-catalytic system as demonstrated in Fig.9. The obtained results revealed that 30 min of binary irradiation US/UV was sufficient to complete the

degradation of 4-NP (20 ppm) using 0.1 g L<sup>-1</sup> of FeVO<sub>4</sub>@CeO<sub>2</sub> in the presence of 10 mM H<sub>2</sub>O<sub>2</sub> at pH = 7. It is obvious that the degradation efficiency of the sonophotocatalytic system was higher than that of the sole sonocatalytic or photocatalytic system by 26% and 13%, respectively, following an order: sonophotocatalytic > photocatalytic > sonocatalytic performance. This remarkable performance can be ascribed to the ability of the US/UV system to exclude all the disadvantages observed in the individual systems, such as the blocking of the catalyst active sites, mass transfer limitations and catalyst fouling [78]. The sonophotocatalytic degradation of 4-NP follows the pseudo first order and the obtained degradation rate for the US/UV system is found to be higher than the sum of the degradation rates of each systems under the same conditions as shown in Table 2 and Fig.S6. To obtain more precise results, the synergistic effect of sonophotocatalytic system, sonocatalysis and photocatalysis degradation of 4-NP was calculated by Eq. (13) [77].

$$\text{synergy (\%)} = \frac{(\mathbf{k}_{\text{sonophotocatalysis}} - (\mathbf{k}_{\text{sonocatalysis}} + \mathbf{k}_{\text{photocatalysis}}))}{\mathbf{k}_{\text{sonophotocatalysis}}} \times 100$$

The data obtained from Table 2 show that the synergetic effect of US/UV system is faster than the sole systems and has a positive effect on 4-NP degradation performance

### 3.3.1. Optimisation of initial pH

To investigate the effect of initial pH on the sonophotocatalytic system, a wide pH range of 2.7 - 11 was screened as shown in Fig.S7. The obtained results revealed that the system was able to completely degrade 4-NP at the different pH values and even within the alkaline pH range after only 30 min of binary irradiation using FeVO<sub>4</sub>@CeO<sub>2</sub>. This remarkable performance shows that the working pH range of FeVO<sub>4</sub>@CeO<sub>2</sub> can be extended to cover the alkaline pH

range (pH = 9). The pKa of 4-NP is 7.15, so it is positively charged at below pH 9 and negatively charged at above pH 9 [79]. Augugliaro et al. [80] reported that the photocatalytic degradation of 4-NP in the presence of TiO<sub>2</sub> decreased by increasing of the solution pH because the negatively charged TiO<sub>2</sub> particles repel the negatively charged 4-NP molecules, which in turn suppress photocatalytic performance. However, using FeVO<sub>4</sub>@CeO<sub>2</sub> within the alkaline pH range, the degradation capability of the system was not reduced. This can be attributed to the presence of V<sup>5+</sup> ion within FeVO<sub>4</sub>, which is deemed a Lewis acid that is able to adsorb OH<sup>-</sup> in the solution and alter the pH of the system [81, 82]. To further explain this outstanding phenomenon with the alkaline pH, the PZCs of the prepared samples were estimated using the mass titration method (Fig.S8). The the PZC of FeVO<sub>4</sub>@CeO<sub>2</sub> is higher than those of FeVO<sub>4</sub> and CeO<sub>2</sub> with values of 9.8, 8.1 and 8.2, respectively. This means that FeVO<sub>4</sub>@CeO<sub>2</sub> particles remain positively charged up to pH 10, so the positively charged FeVO<sub>4</sub>@CeO<sub>2</sub> particles will be able to attract the negatively charged 4-NP molecules at the alkaline pH. This remarkable enhancement in the PZC value can be ascribed to the presence of Ce<sup>3+</sup> ions that induces more defects in FeVO<sub>4</sub> crystals. The presence of such defects enhances the adsorption of hydroxyl species on the particles surface and then increases the affinity towards protons, which in turn increases the value of PZC [83].The enhanced PZC reveals that the surface of the catalyst is highly susceptible to be positively charged, and so attracting the negatively charged molecules [84,85].

### *3.4. Reusability*

The sonophotocatalytic stability and reusability of FeVO<sub>4</sub>@CeO<sub>2</sub> was investigated throughout six successive cycles under the same operating conditions (Fig.10). The sonophotocatalytic performance slightly decreased after six cycles. The synergic effect between FeVO<sub>4</sub> core and CeO<sub>2</sub> shell (Fig.7 (a, b)) can enhance stability toward 4-NP degradation.

Furthermore, to identify the change in the structure and morphological stability, the XRD after the first and sixth runs and the SEM of FeVO<sub>4</sub>@CeO<sub>2</sub> after six runs were scrutinised (Fig.S9 and S10).

### 3.5. TOC and mineralisation

The mineralisation performances of the materials, TOC analyses, were examined (Fig.S11). FeVO<sub>4</sub>@CeO<sub>2</sub> sonophotocatalyst possesses a high mineralisation capacity for the removal of 4-NP, reaching 92.2% in 30 min. The remarkable achievement of the sonophotocatalytic performance of the FeVO<sub>4</sub>@CeO<sub>2</sub> can be attributed to its high adsorption rate, fast mass diffusion and enhanced performance of electron–holes pairs with a high generation rate of hydroxyl and superoxide radicals. The formed intermediates need longer time degrade completely, due to their slower rate of reaction with hydroxyl radicals attacking [86].

### 3.6. Radical scavengers

The pathway of the 4-NP sonophotocatalytic degradation by radical trapping was executed to investigate the main active species in the reaction (Fig.11). In this study, isopropanol (40 mmol L<sup>-1</sup>), ethylene diamine tetraacetic acid (40 mmol L<sup>-1</sup>), benzoquinone (4 mmol L<sup>-1</sup>), and potassium dichromate (2 mmol L<sup>-1</sup>) were used to trap hydroxyl radicals (<sup>•</sup>OH), holes (h<sup>+</sup>), superoxide radicals (<sup>•</sup>O<sub>2</sub><sup>-</sup>) and electron (e<sup>-</sup>), respectively. The sonophotocatalytic performance is greatly inhibited with a slight difference by adding IPA, EDTA and BQ in comparison with the initial activity in the absence of radical scavengers, and follows the order <sup>•</sup>OH > h<sup>+</sup> > O<sub>2</sub><sup>•-</sup>. On the other hand, the degradation performance is highly enhanced by adding potassium dichromate, which acts as a trapping agent for the generated electrons and thus extends the lifetime of the holes.

## Conclusions

Core shell nanostructured  $\text{FeVO}_4@\text{CeO}_2$  acted as effective Fenton-like achieve high performance in the sonophotocatalytic degradation of 4-NP at low concentrations of the catalyst and oxidant. The synergistic effect of  $\text{FeVO}_4@\text{CeO}_2$  enlarges the photoactivity of  $\text{FeVO}_4$  and effectively inhibits the charge carrier recombination, ultimately improving the photocatalytic activity of  $\text{FeVO}_4$  with  $\text{CeO}_2$ . The hydroxyl radicals ( $\cdot\text{OH}$ ) and holes ( $\text{h}^+$ ) play a more important role than that of super oxide radicals ( $\text{O}_2^{\cdot-}$ ) in the degradation process. This paper therefore opens up the prospect of further exploration of novel and interesting core-shell nanostructures for environmental remediation.

## References

- [1] Herrera-Melián, J.A.; Martín-Rodríguez, A.J.; Ortega-Méndez, A.; Araña, J.; Doña-Rodríguez, J.M.; Pérez-Peña, J. Degradation and detoxification of 4-nitrophenol by advanced oxidation technologies and bench-scale constructed wetlands. *J. Environ. Manage.* **2012**, *105* (30) 53–60.
- [2] Yehia, F.Z.; Eshaq, Gh.; ElMetwally, A.E. Enhancement of the working pH range for degradation of p-nitrophenol using  $\text{Fe}^{2+}$ -aspartate and  $\text{Fe}^{2+}$ -glutamate complexes as modified Fenton reagents. *Egypt. J. Pet.* **2016**, *25* (2) 239–245.
- [3] Lunhong, Ai; Jing, J. Catalytic reduction of 4-nitrophenol by silver nanoparticles stabilised on environmentally benign macroscopic biopolymer hydrogel, Short Communication. *Bioresource technology.* **2013**, *132* (22) 374-377.
- [4] Peretz, S.; Cinteza, O. Removal of some nitrophenol contaminants using alginate gel beads.
- [5] Mishra, K.P.; Gogate, P.R. Intensification of sonophotocatalytic degradation of p-nitrophenol at pilot scale capacity. *Ultrason. Sonochem.* **2011**, *18* (3) 739-744.
- [6] Erick, R.B.; Dolores, M.; Evaristo, M.; Dionysios, D. Degradation of microcystin-LR, toxin by Fenton and Photo-Fenton processes. *Toxicon.* **2004**, *43* (7) 829–832.
- [7] Ricardo, A.; Efrain, A. Advanced Oxidation Processes for Waste Water Treatment, *Emerging Green Chemical Technology*. Chapter 7 – Sonolysis. **2018**, 177-213.

- [8] Slimane, M.; Oualid, H.; Fethi, S.; Mahdi, C. Sonochemical degradation of Rhodamine B in aqueous phase: Effects of additives, *Chemical Engineering Journal*, **2010**, *158* (3) 550–557.
- [9] Gogat, P.R. Treatment of wastewater streams containing phenolic compounds using hybrid techniques based on cavitation: A review of Current Status and the way Forward. *Ultrason. sonochem.* **2008**, *15* (1) 1-15.
- [10] Bagal, M.V.; Gogate, P.R. Wastewater treatment using hybrid treatment schemes based on cavitation and Fenton chemistry: a review. *Ultrason. Sonochem.* **2014**, *21* (1) 1-14.
- [11] Chilukoti, B. S.; Vijayanand, M.; Aniruddha, B.P. ; Muthupandian, A. Mechanistic Investigations on Sonophotocatalytic Degradation of Textile Dyes with Surface Active Solutes. *Ind. Eng. Chem. Res.* **2011**, *50* (20) 11485–11494.
- [12] ElShafei, G. M. S.; Al-Sabagh, A. M.; Yehia, F. Z.; Philip, C. A.; Moussa, N. A.; Eshaq, Gh.; ElMetwally, A. E.; Metal oxychlorides as robust heterogeneous Fenton catalysts for the sonophotocatalytic degradation of 2-nitrophenol. *Appl. Catal. B Environ.* **2018**, *224* (28) 681-691.
- [13] Zaleska, A.; Marchelek, M.; Diak, M.; Grabowska, E. Noble metal-based bimetallic nanoparticles: the effect of the structure on the optical, catalytic and photocatalytic properties. *Adv. Colloid Interf. Sci.* **2016**, *229* (4) 80–107.
- [14] Mitsudome, T.; Kaneda, K. Advanced core-shell nanoparticle catalysts for efficient organic transformations. *Chem. Cat. Chem.* **2013**, *5* (7) 1681–1691.
- [15] Zhang, M.; Sheng, Q.; Nie, F.; Zheng, J. Synthesis of Cu nanoparticles-loaded Fe<sub>3</sub>O<sub>4</sub>@carbon core-shell nanocomposite and its application for electrochemical sensing of hydrogen peroxide. *J. electroanal. chem.* **2014**, *730* (2) 10-15
- [16] Pham, V.L.; Kim, D-G.; Ko, S-O. Oxidative degradation of the antibiotic oxytetracycline by Cu@Fe<sub>3</sub>O<sub>4</sub> core-shell nanoparticles. *Sci. Total Environ.* **2018**, *631–632* (26) 608–618.
- [17] Siadatnasab, S. F.; Khataee, A. Ultrasound-assisted degradation of organic dyes over magnetic CoFe<sub>2</sub>O<sub>4</sub>@ZnS core-shell nanocomposite. *Ultrason Sonochem.* **2017**, *37* (11) 298-309.
- [18] Shah, NH. ; Bhangonkar, KR.; Pinjari, DV. ; Mhaske, ST. Ultrasonically Engineered Ceria-Titania Nanostructure Mediated Photocatalytic and Sonocatalytic Degradation of Organic Dye, *Austin Chem Eng.* **2016**, *3* (3) 1032-2016.
- [19] Pham, V.L.; Kim, S. Ko. Cu@Fe<sub>3</sub>O<sub>4</sub> core-shell nanoparticle-catalyzed oxidative degradation of the antibiotic oxytetracycline in pre-treated landfill leachate, *Chemosphere.* **2018**, *191* (31) 639-650.

- [20] Khanchandani, S.; Kumar, S.; Ashok, S. K.; Ganguli, A.K. Comparative Study of TiO<sub>2</sub>/CuS Core/Shell and Composite Nanostructures for Efficient Visible Light Photocatalysis, *ACS Sustainable Chem. Eng.* **2016**, *4* (3) 1487–1499.
- [21] Ding, M.; Yao, N.; Wang, C.; Huang, J. ; Shao, M. ; Zhang, S.; Li, P. ; Deng, X. ; Xu, X. ZnO@CdS Core-Shell Heterostructures: Fabrication, Enhanced Photocatalytic, and Photoelectrochemical Performance, *Nanoscale Res Lett.* **2016**, *11*(1) 205-211.
- [22] Kanmani, S.S.; Ramachandran, K. Synthesis and characterisation of TiO<sub>2</sub>/ZnO core/shell nanomaterials for solar cell applications, *Renewable Energy.* **2012**, *43* (C) 149-156.
- [23] He, G-H. ; He, G-L.; Li, A-J.; Li, X.; Wang, X-J. ; Fang, Y-P. ; Xu, Y-H. Synthesis and visible light photocatalytic behavior of WO<sub>3</sub> (core)/Bi<sub>2</sub>WO<sub>6</sub> (shell). *Journal of Molecular Catalysis A: Chemical.* **2014**, *385* (4) 106-111.
- [24] Habila, M.A.; AlOthman, Z.A.; El-Toni, A.M.; Labis, J.P. ; Soylak, M. Synthesis and application of Fe<sub>3</sub>O<sub>4</sub>@SiO<sub>2</sub>@TiO<sub>2</sub> for photocatalytic decomposition of organic matrix simultaneously with magnetic solid phase extraction of heavy metals prior to ICP-MS analysis. *Talanta*, **2016**, *154* (23) 539-547.
- [25] Zheng, X.; Huang, M.; You, Y.; Peng, H.; Wen, J. Core-shell structured  $\alpha$ -Fe<sub>2</sub>O<sub>3</sub>@CeO<sub>2</sub> heterojunction for the enhanced visible-light photocatalytic activity. *Mater. Res. Bull.* **2018**, *101* (12) 20-28.
- [26] Huang, B.; Yu, D.; Sheng, Z.; Yang, L.; Novel CeO<sub>2</sub>@TiO<sub>2</sub> core-shell nanostructure catalyst for selective catalytic reduction of NO<sub>x</sub> with NH<sub>3</sub>. *J. Environ Sci.* **2017**, *55* (25) 129-136.
- [27] Hu, S. ; Zhou, F. ; Wang, L. ; Zhang, J. Preparation of Cu<sub>2</sub>O/CeO<sub>2</sub> heterojunction photocatalyst for the degradation of Acid Orange 7 under visible light irradiation. *Catal. Commun.* **2011**, *12* (9) 794-797.
- [28] Li, S.; Wang, F.; Wang, S.; Zhou, H.; Li, H. Synthesis of buckhorn-like BiVO<sub>4</sub> with a shell of CeO<sub>x</sub> nanodots: Effect of heterojunction structure on the enhancement of photocatalytic activity. *Appl. Catal. B. environ.* **2015**, *170* (7) 186-194.
- [29] Khanchandani, S.; Srivastava, P. ; Kumar, S. ; Ghosh, S.; Ganguli, A. Band Gap Engineering of ZnO using Core/Shell Morphology with Environmentally Benign Ag<sub>2</sub>S Sensitizer for Efficient Light Harvesting and Enhanced Visible-Light Photocatalysis. *Inorg. Chem.* **2014**, *53* (17) 8902–8912.
- [30] Ghows, N.; Entezari, M.; Sono-synthesis of core-shell nanocrystal (CdS/TiO<sub>2</sub>) without surfactant. *Ultrason. Sonochem.* **2012**, *19* (5) 1070-1078.

- [31] Ijaz, S.; Ehsan, M.F.; Ashiq, M.N; Karamat, N.; He, T. Preparation of CdS@CeO<sub>2</sub> core/shell composite for photocatalytic reduction of CO<sub>2</sub> under visible-light irradiation. *Appl.Surf. Sci.*, **2016**, 390 (20) 550-559.
- [32] Chae, B.W.; Amna, T.; Hassan, M.S.; Al-Deyab, S.S.; Khil, M.S. CeO<sub>2</sub>-Cu<sub>2</sub>O composite nanofibers: synthesis, characterisation photocatalytic and electrochemical application. *Adv. Powd. Technol.* **2017**, 28 (1) 230–235.
- [33] Zhang, P. ; Liu, Y.; Tian, B. ; Luo, Y. ; Zhang, J. Synthesis of core-shell structured CdS@CeO<sub>2</sub> and CdS@TiO<sub>2</sub> composites and comparison of their photocatalytic activities for the selective oxidation of benzyl alcohol to benzaldehyde. *Catal. Today*, **2017**, 281 (26) 181–188.
- [34] Chen, F.; Ho, P.; Ran, R.; Chen, W.; Si, Z.; Wu, X.; Weng, D. ; Huang, Z.; Lee, C. Synergistic effect of CeO<sub>2</sub> modified TiO<sub>2</sub> photocatalyst on the enhancement of visible light photocatalytic performance. *J. Alloy.Comp.* **2017**, 714 (15) 560–566.
- [35] Cargnello, M.; Wieder, N.; Montini, T. ; Gorte, R.; Fornasiero, P. Synthesis of Dispersible Pd@CeO<sub>2</sub> Core–Shell Nanostructures by Self-Assembly. *J. Am. Chem. Soc.*, **2010**, 132 (4) 1402–1409.
- [36] Hosseinpour-Mashkani, S.M.; Sobhani-Nasab, A.; Maddahfar, M. Synthesis, Characterisation and Investigation Magnetic and Photovoltaic Properties of FeVO<sub>4</sub> Nanoparticles, *J. Nanostruct.* **2016**, 6 (1) 70-73.
- [37] Kaneti, Y.; Zhang, Z.; Yue, J.; Jiang, X.; Yu, A. Porous FeVO<sub>4</sub> nanorods: synthesis, characterisation, and gas-sensing properties toward volatile organic compounds. *J Nanopart Res.* **2013**, 15 (8) 1948-1963.
- [38] Krishnamoorthy, K.; Veerapandian, M.; Zhang, L-H. ; Yun, K.; Kim, S.J. Surface chemistry of cerium oxide nanocubes: Toxicity against pathogenic bacteria and their mechanistic study. *J. Ind. Eng. Chem.*, 2014, 20 (5) 3513-3517.
- [39] Zheng, X.; Huang, M.; You, Y.; Peng, H.; Wen, J. Core-shell structured  $\alpha$ -Fe<sub>2</sub>O<sub>3</sub>@CeO<sub>2</sub> heterojunction for the enhanced visible-light photocatalytic activity, *Mater res bull*, **2018**, 101 (12) 20-28.
- [40] Franca, A.S.; Oliveira, L.S.; Ferreira, M.E. Kinetics and equilibrium studies of methylene blue adsorption by spent coffee grounds, *Desalination*. **2009**, 249 (1) 267-272.
- [41] Vuk, A.; Orel, B.; Draz'ic, G. IR spectroelectrochemical studies of Fe<sub>2</sub>V<sub>4</sub>O<sub>13</sub>, FeVO<sub>4</sub> and InVO<sub>4</sub> thin films obtained via sol–gel synthesis. *J Solid State Electrochem.* **2001**, 5 (7-8) 437–449.
- [42] Nithya, V.D. ; Kalai Selvan, R. ; Sanjeeviraja, C.; Mohan Radheep, D.; Arumugam, S. Synthesis and characterisation of FeVO<sub>4</sub> nanoparticles. *Mar. Res. Bull.* **2011**, 46 (10) 1654-1658.

- [43] Ansari, A.A. ; Solanki, P.R. ; Malhotra, B.D. Hydrogen peroxide sensor based on horse radish peroxidase immobilised nanostructured cerium oxide film. *J. Biotechnol.* **2009**, *142* (2) 179-184.
- [44] Lehnen, T.; Valldor, M.; Nižňanský, D.; Mathur, S. Hydrothermally grown porous FeVO<sub>4</sub> nanorods and their integration as active material in gas-sensing Devices. *Mater.Chem. A.* **2014**, *2* (6) 1862–1868.
- [45] Fan, Z.; Meng, F.; Gong, J.; Li, H.; Hu, Y. ; Liu, D. Enhanced photocatalytic activity of hierarchical flower-like CeO<sub>2</sub>/TiO<sub>2</sub> heterostructures, *Materials Letters.* **2016**, *175* (7) 36-39.
- [46] Sing, K. S. W; Everett, D. H.; Haul, R. A. W. ; Moscou, L. ; Pierotti, R. A. ; Rouquerol, J.; Siemieniewska, T. Reporting Physisorption data for Gas/Solid Systems with Special Reference to the determination of surface area and porosity. *Pure Appl. Chem.* **1985**, *57* (4) 603-619.
- [47] Cao, J.; Xu, B. ; Lin, H.; Luo, B. ; Chen, S. Chemical etching preparation of BiOI/BiOBr heterostructures with enhanced photocatalytic properties for organic dye removal , *J. Chem. Eng.* **2012**, *185-186* (10) 91-99.
- [48] Li, K.; Gao, S. M. ; Wang, Q. Y. ; Xu, H.; Wang, Z. Y. ; Huang, B. B. ; Dai, Y.; Lu, J. In-Situ-Reduced Synthesis of Ti<sup>3+</sup> Self-Doped TiO<sub>2</sub>/ g-C<sub>3</sub>N<sub>4</sub> Heterojunctions with High Photocatalytic Performance under LED Light Irradiation. *ACS Appl. Mater. Interfaces*, **2015**, *7* (17) 9023–9030.
- [49] Saranya, J.; Ranjith, K.S.; Saravanan, P.; Mangalaraj, D.; Kumar, R. Cobalt-doped cerium oxide nanoparticles: Enhanced photocatalytic activity under UV and visible light irradiation, *Mater. Sci. Semicond. Process.* **2014**, *26* (99) 218–224.
- [50] Choudhury, B. ; Chetri, P. ; Choudhury, A. Oxygen defects and formation of Ce<sup>3+</sup> affecting the photocatalytic performance of CeO<sub>2</sub> Nanoparticles, *RSC Adv.*, **2014**, *4* (9) 4663–4671.
- [51] Zhang, K.-L. ; Liu, C.-M. ; Huang, F.-Q. ; Zheng, C.; Wang, W.-D. Study of the electronic structure and photocatalytic activity of the BiOCl photocatalyst, *Appl. Catal. B: Environ.* **2006**, *68* (3-4) 125-129.
- (52) Tomova, D.; Iliev, V.; Eliyas, A.; Rakovsky, S. Promoting the Oxidative Removal Rate of Oxalic Acid on Gold-Doped CeO<sub>2</sub>/TiO<sub>2</sub> Photocatalysts under UV and Visible Light Irradiation. *Sep. Purif. Technol.* **2015**, *156* (2) 715–723.
- [53] Balamurugan, M.; Yun, G.; Ahn, K.-S. ; Kang, S. H. Revealing the Beneficial Effects of FeVO<sub>4</sub> Nanoshell Layer on the BiVO<sub>4</sub> Inverse Opal Core Layer for Photoelectrochemical Water Oxidation. *J. Phys. Chem.* **2017**, *121* (14) 7625–7634.

- [54] Yang, W.; Tan, G.Q.; Huang, J.; Ren, H.J.; Xia, A.; Zhao, C.C. Enhanced magnetic property and photocatalytic activity of UV-light responsive N-doped Fe<sub>2</sub>O<sub>3</sub>/FeVO<sub>4</sub> heterojunction. *Ceram. Int.* **2015**, *41* (1) 1495–1503.
- [55] Futsuhara, M.; Yoshioka, K.; Takai, O. Optical properties of zinc oxynitride thin films. *Thin Solid Films.* **1998**, *317* (1) 322–325.
- [56] Tsunekawa, S.; Fukuda, T.; Kasuya, A. X-ray photoelectron spectroscopy of monodispersed CeO<sub>2</sub>x nanoparticles. *Surf. Sci.* **2000**, *457* (3) L437–L440.
- [57] Krishnamoorthy, K.; Veerapandian, M.; Zhang, L.-H.; Yun, K.; Kim, S.J. Surface chemistry of cerium oxide nanocubes: Toxicity against pathogenic bacteria and their mechanistic study, *J. Ind. Eng. Chem.* **2014**, *20* (5) 3513–3517.
- [58] Guo, X. L.; Li, J.; Zhou, R. X. Catalytic Performance of Manganese Doped CuO-CeO<sub>2</sub> Catalysts for Selective Oxidation of CO in Hydrogen-Rich Gas. *Fuel*, **2016**, *163* (9) 56–64.
- [59] Petrier, C.; Lamy, M.-F.; Francony, A.; Benahcene, A.; David, B.; Renaudin, V.; Gondrexon, N. Sonochemical degradation of phenol in dilute aqueous solutions: comparison of the reaction rates at 20 and 487 kHz. *J. Phys. Chem.* **1994**, *98* (41) 10514–10520.
- [60] Henglein, A. Chemical effects of continuous and pulsed ultrasound in aqueous solutions. *Ultrason. Sonochem.* **1995**, *2* (2) S115–S121.
- [61] Mehrdad, A.; Hashemzadeh, R. Ultrasonic degradation of rhodamine B in the presence of hydrogen peroxide and some metal oxide. *Ultrason. Sonochem.* **2010**, *17* (1) 168–172.
- [62] Abbasi, M.; Asl, N.R. Sonochemical degradation of Basic Blue 41 dye assisted by nanoTiO<sub>2</sub> and H<sub>2</sub>O<sub>2</sub>. *J. Hazard. Mater.* **2008**, *153* (3) 942–947.
- [63]. Kwan, W. P; Voelker, B. M. Rates of hydroxyl radical generation and organic compound oxidation in mineral-catalyzed fenton-like systems. *Environ. Sci. Technol.*, **2003**, *37* (6) 1150–1158.
- [64] Khaliullin, R.Z.; Bell, A.T.; Head-Gordon, M. A density functional theory study of the mechanism of free radical generation in the system vanadate/PKA/H<sub>2</sub>O<sub>2</sub>. *J. Phys. Chem. B.* **2005**, *109* (38) 17984–17992.
- [65] Kozlov, Y.N.; Nizova, G.V.; Shul'pin, G.B. Oxidations by the reagent O<sub>2</sub>-H<sub>2</sub>O<sub>2</sub> vanadium derivative-pyrazine-2-carboxylic acid: Part 14. Competitive oxidation of alkanes and acetonitrile (solvent), *J. Mol. Catal. A: Chem.* **2005**, *227* (1-2) 247–253.
- [66] Bokare, A.D.; Choi, W. Review of iron-free Fenton-like systems for activating H<sub>2</sub>O<sub>2</sub> in advanced oxidation processes, *J. Hazard. Mater.* **2014**, *275* (8) 121–135.

- [67] Heckert, E.G. ; Seal, S.W.T. Self, Fenton-like reaction catalyzed by the rare earth inner transition metal cerium, *Environ. Sci. Technol.* **2008**, *42* (13) 5014–5019.
- [68] Wetchakun, N.; Chaiwichain, S.; Inceesungvorn, B.; Pingmuang, K.; Phanichphant, S.; Minett, A. I.; Chen, J. BiVO<sub>4</sub>/CeO<sub>2</sub> Nanocomposites with High Visible-Light-Induced Photocatalytic Activity. *ACS Appl. Mater. Interfaces.* **2012**, *4* (7) 3718–3723.
- [69] Huang, H. W. ; Liu, L. Y. ; Zhang, Y. H. ; Tian, N. Novel BiIO<sub>4</sub>/ BiVO<sub>4</sub> Composite Photocatalyst with Highly Improved Visible-Light-Induced Photocatalytic Performance for Rhodamine B Degradation and Photocurrent Generation. *RSC Adv.* **2015**, *5* (2) 1161–1167.
- [70] Luo, Z. ; Poyraz, A. S. ; Kuo, C. H. ; Miao, R.; Meng, Y. T. ; Chen, S. Y. ; Jiang, T.; Wenos, C. ; Suib, S. L. Crystalline Mixed Phase (Anatase/Rutile) Mesoporous Titanium Dioxides for Visible Light Photocatalytic Activity. *Chem. Mater.* **2015**, *27* (1) 6–17.
- [71] Jiang, Z.; Liu, Y.; Jing, T.; Huang, B.; Zhang, X.; Qin, X.; Dai, Y.; Whangbo, M-H. Enhancing the Photocatalytic Activity of BiVO<sub>4</sub> for Oxygen Evolution by Ce Doping: Ce<sup>3+</sup> Ions as Hole Traps. *J. Phys. Chem. C.* **2016**, *120* (4) 2058–2063.
- [72] Chen, L. ; Meng, D. ; Wu, X.; Wang, A. ; Wang, J. ; Wang, Y.; Yu, M. In Situ Synthesis of V<sup>4+</sup> and Ce<sup>3+</sup> Self-Doped BiVO<sub>4</sub>/CeO<sub>2</sub> Heterostructured Nanocomposites with High Surface Areas and Enhanced Visible-Light Photocatalytic Activity. *J. Phys. Chem. C.* **2016**, *120* (33) 18548–18559.
- [73] Malato, S.; Blanco, J.; Maldonado, M.; Fernández-Ibáñez, P.; Campos, A. Optimising solar photocatalytic mineralisation of pesticides by adding inorganic oxidising species; application to the recycling of pesticide containers. *Appl. Catal. B: Environ.* **2000**, *28* (3-4)163-174.
- [74] A.E. ElMetwally, G.h. Eshaq, A.M. Al-Sabagh, F.Z. Yehia, C.A. Philip, N.A. Moussa, G.M.S. ElShafei, Insight into heterogeneous Fenton-sonophotocatalytic degradation of nitrobenzene using metal oxychlorides. *Sep. Purif. Technol.* **2019**, *210* (36) 452–462.
- [75] Pang, Y.L.; Abdullah, A.Z.; Fe<sup>3+</sup> doped TiO<sub>2</sub> nanotubes for combined adsorption–sonocatalytic degradation of real textile wastewater. *Appl. Catal. B.* **2013**, *129* (13) 473–481.
- [76] Pang, Y.L.; Abdullah, A.Z.; Bhatia, S. Review on sonochemical methods in the presence of catalysts and chemical additives for treatment of organic pollutants in wastewater. *Desalination* **2011**, *277* (1-3) 1–14.
- [77] Verma, A.; Kaur, H.; Dixit, D. Photocatalytic, sonolytic and sonophotocatalytic degradation of 4-chloro-2-nitro phenol. *Arch. Environ. Prot.* **2013**, *39* (2) 17-28.
- [78] Gogate, P.R.; Pandit, A.B. Sonophotocatalytic reactors for wastewater treatment: A critical review. *AIChE journal.* **2004**, *50* (5) 1051-1079.

- [79] Ahn, W-Y. ; Sheeley, S.A.; Rajh, T.; Cropek, D.M. Photocatalytic reduction of 4-nitrophenol with arginine-modified titanium dioxide nanoparticles. *Appl. Catal. B: Environ.* **2007**, *74* (1-2) 103–110.
- [80] Augugliaro, V.; Lopezmunoz, M.J.; Palmisano, L.; Soria, J. Influence of pH on the degradation kinetics of nitrophenol isomers in a heterogeneous photocatalytic system. *Appl. Catal. A.* **1993**, *101* (1) 7–13.
- [81] Rossetti, I.; Fabbrini, L. ; Ballarini, N. ; Oliva, C.; Cavani, F. ; Cericola, A.; Bonelli, B. ; Piumetti, M.; Garrone, E. ; Dyrbeck, H.; Blekkan, E A. ; Forni, L. V–Al–O catalysts prepared by flame pyrolysis for the oxidative dehydrogenation of propane to propylene. *Catal.Today*, **2009**, *141* (3-4) 271–281.
- [82] Ou, X.; Yan, J.; Zhang, F.; Zhang, C. Accelerated degradation of orange G over a wide pH range in the presence of FeVO<sub>4</sub>. *Front. Env. Sci. Eng.* **2018**, *12* (7) 1-7.
- [83] Deiana, C.; Fois, E.; Coluccia, S.; Martra, G. Surface Structure of TiO<sub>2</sub> P25 Nanoparticles: Infrared Study of Hydroxy Groups on Coordinative Defect Sites. *J. Phys. Chem. C.* **2010**, *114* (49) 21531–21538.
- [84] Chai, L.; Wang, Y.; Zhao, N.; Yang, W. ; You, X. Sulfate-doped Fe<sub>3</sub>O<sub>4</sub>/Al<sub>2</sub>O<sub>3</sub> nanoparticles as a novel adsorbent for fluoride removal from drinking water. *Water Res.*, **2013**, *47* (12) 4040–4049
- [85] Mohapatra, M.; Sahoo, S.; Anand, S.; Das, R. Removal of As (V) by Cu(II)-, Ni(II)-, or Co(II)-doped goethite samples. *J. Colloid Interface Sci.*, **2006**, *298* (1) 6–12.
- [86] Wang, K-H.; Hsieh, Y-H. ; Chen, L-J. The heterogeneous photocatalytic degradation intermediates and mineralisation for the aqueous solution of cresols and nitrophenols. *J. Hazard. Mater.* **1998**, *59* (28) 251–260.